Elastic Full Waveform Inversion of VSP Data from a Complex Anticline in Northern Iraq

Zhaolun Liu[1], Jürgen Hoffmann[2], Frederik J. Simons[1], and Jeroen Tromp[1]
[1]Princeton University, [2]DNO ASA

SUMMARY

We demonstrate an application of isotropic elastic Full-Waveform Inversion (FWI) to a field data set of Vertical Seismic Profiles (VSP) from a structurally complex narrow anticline in Northern Iraq. A practical elastic FWI workflow is developed to invert offset VSP seismic data. Synthetic tests indicate that this approach can give accurate wave speed updates for the target anticlinal structure. We use inverted wave speed models to perform elastic Reverse-Time Migration (RTM) of the data. The RTM results show that the shear wave speed (V_S) image has a higher resolution than the compressional speed (V_P) image for the target structure, owing to the presence of interpretable P-to-S converted waves. The results of the field test show that elastic FWI produces elastic models from which we obtain clear V_S images of the thrust fault of interest.

INTRODUCTION

We study a structurally complex area where outcropping Cenozoic carbonates are folded over low-wave-speed clastic sediments and a thrust-deformed core of Mesozoic carbonates. A V_P model is shown in Fig. 1a. Of specific interest are the high wave speed Cretaceous carbonates and the sediments above and below. The strong topography and complex overburden with strong vertical and lateral wave speed variations stand in the way of procuring clean images for our region of interest, at least with current surface seismic data processing techniques. A Vertical Seismic Profile (VSP) survey can provide relatively noise-free data by lowering the recording device down a borehole (Hinds et al., 1996). In our case, the borehole does penetrate the high wave speed carbonate body, and the VSP data have the potential to deliver the required solution.

Our survey comprises two wells, W1 and W2. For each, one rig-source and three offset-source VSP surveys were conducted, with three-component accelerometer recordings. The locations of the sources and receivers are shown in Fig. 1b. The initial VSP data analysis consisted of ray-based traveltime modeling of mainly direct and P-to-P reflected waves for the rig-source data. Various parts of the VSP wavefield (e.g., amplitudes, converted waves, prism waves) were initially poorly understood and therefore not used in the analysis, particularly from the offset VSP data.

To get a model that can accurately explain the complex multi-component wavefield, we apply elastic FWI (e.g. Lailly, 1983; Tarantola, 1984; Pérez Solano and Plessix, 2019; Borisov et al., 2020; Murphy et al., 2020) to the offset VSP dataset. We detail a practical elastic FWI workflow to invert the offset VSP seismic data for the target wave speed structure. The workflow is demonstrated by using both synthetic and real data. The estimated elastic wave speed models were used to migrate the data by elastic reverse-time migration (RTM), yielding a V_S image better resolved than V_P, thanks to the P-to-S conversions.

METHODOLOGY

The elastic FWI method inverts for the P- and S-wave speed models V_P and V_S in the elastic model-parameter vector $\mathbf{m}$, for example, by minimizing the least-squares waveform misfit function (Tromp et al., 2005),

$$\chi(\mathbf{m}) = \sum_{s=1}^{N_s}\sum_{r=1}^{N_r}\int_0^T \frac{1}{2}||\mathbf{u}(\mathbf{x}_r,\mathbf{x}_s,t;\mathbf{m}) - \mathbf{d}(\mathbf{x}_r,\mathbf{x}_s,t)||^2 \mathrm{d}t, \quad (1)$$

where $\mathbf{d}(\mathbf{x}_r,\mathbf{x}_s,t)$ represents observed multi-component waveform data at receivers $\mathbf{x}_r$, $r = 1,\ldots,N_r$, and for sources at $\mathbf{x}_s$, $s = 1,\ldots,N_s$, and with $\mathbf{u}(\mathbf{x}_r,\mathbf{x}_s,t;\mathbf{m})$ being the corresponding synthetic data, computed in model $\mathbf{m}$. The misfit function in eq. (1) is very sensitive to amplitude errors in the data, so that the inversion can easily get stuck in local minima. To make the inversion less sensitive to such amplitude errors, we use a normalized crosscorrelation misfit function (Sen and Stoffa, 1990; Choi and Alkhalifah, 2012),

$$\tilde{\chi}(\mathbf{m}) = -\sum_{i=1}^{N_s}\sum_{j=1}^{N_r}\tilde{\mathbf{u}}_{i,j}\cdot\tilde{\mathbf{d}}_{ij}, \quad (2)$$

where $\tilde{\mathbf{d}}_{i,j} = \mathbf{d}_{i,j}/||\mathbf{d}_{i,j}||$ and $\mathbf{d}_{i,j}$ are the trace vectors observed at receivers $\mathbf{x}_j$ for sources at $\mathbf{x}_i$, and $\tilde{\mathbf{u}}_{i,j} = \mathbf{u}_{i,j}/||\mathbf{u}_{i,j}||$ are the synthetic trace vectors. The gradient of $\tilde{\chi}(\mathbf{m})$ with respect to a model parameter m_l is,

$$\frac{\partial\tilde{\chi}(\mathbf{m})}{\partial m_l} = \sum_{i=1}^{N_s}\sum_{j=1}^{N_r}\frac{\partial \mathbf{u}_{i,j}}{\partial m_l}\cdot\frac{1}{||\mathbf{u}_{i,j}||}[(\tilde{\mathbf{u}}_{i,j}\cdot\tilde{\mathbf{d}}_{ij})\tilde{\mathbf{u}}_{i,j} - \tilde{\mathbf{d}}_{ij}]. \quad (3)$$

The optimal model parameters m_l are obtained by gradient-update methods. For example, the steepest-descent formula is

$$m_l^{(k+1)} = m_l^{(k)} - \alpha\frac{\partial\tilde{\chi}(\mathbf{m})}{\partial m_l}, \quad (4)$$

where α is a step length, and the parenthetical superscript (k) denotes the kth iteration. In practice, the L-BFGS method is used for faster convergence (Nocedal and Wright, 2006).

The elastic FWI method is non-linear and suffers from cycle skipping which makes it get stuck easily in local minima. To mitigate the cycle skipping problem, we implement the elastic FWI following the workflow in Fig. 2. After preprocessing the raw data, we build an initial model by elastic traveltime inversion of the first breaks. Subsequently, we obtain the Source Time Function (STF), if it is not already available, estimated by solving a linear inverse problem of which the solution in the frequency domain is given by

$$\mathbf{s}_{\mathrm{STF}}(\omega) = \sum_{s=1}^{N_s}\sum_{r=1}^{N_r}\frac{\hat{\mathbf{g}}^*(\mathbf{x}_r,\mathbf{x}_s,\omega;\mathbf{m}_0)\cdot\hat{\mathbf{d}}(\mathbf{x}_r,\mathbf{x}_s,\omega)}{\hat{\mathbf{g}}^*(\mathbf{x}_r,\mathbf{x}_s,\omega;\mathbf{m}_0)\cdot\hat{\mathbf{g}}(\mathbf{x}_r,\mathbf{x}_s,\omega;\mathbf{m}_0)}, \quad (5)$$

10.1190/segam2021-3582871.1

where $\hat{\mathbf{g}}(\mathbf{x}_r, \mathbf{x}_s, \omega; \mathbf{m}_0)$ denotes the Green functions at receiver $\mathbf{x}_r$ for sources at $\mathbf{x}_s$ computed in the starting model $\mathbf{m}_0$. Furthermore, $\hat{\mathbf{d}}(\mathbf{x}_r, \mathbf{x}_s, \omega)$ denotes the observed data in the frequency domain and the superscript $*$ represents complex conjugation. Next, we apply elastic FWI to the early-arriving waveforms (within 1.5 dominant wavelengths). During the early-arrival FWI, we use the multiscale strategy (Bunks et al., 1995), which successively inverts subportions of the dataset of increasingly higher frequency content, since low-frequency records are less sensitive to cycle-skipping artifacts. At the same time we update the STF, which has been shown to significantly improve the inversion effectiveness on field data (Borisov et al., 2020). After early-arrival FWI, we reduce data muting to proceed to FWI of the late arrivals, whereby we maintain the multiscale strategy and carry out STF updates. We may repeat FWI by reducing data muting step by step.

The elastic FWI workflow is carried out by SeisFlows (Modrak et al., 2018), a Python-based open-source package. SeisFlows uses the open-source spectral-element method SPECFEM2D to perform forward simulation (Komatitsch and Tromp, 1999), which handles strong surface topography exceptionally well.

A REALISTIC SYNTHETIC EXAMPLE

Before applying the elastic FWI method to the real data, we carried out 2D synthetic tests using the same acquisition geometry as the actual offset-VSP survey. Figs 3a and 3b show the true and initial V_P models for the elastic FWI tests. White dots and lines represent the locations of the three sources and 264 receivers, respectively. The V_S model is the scaled $V_S(\mathbf{x}) = V_P(\mathbf{x})/1.732$. We create initial *P*- and *S*-wave speed models by smoothing the true models while the wave speeds in the radius of 500 m around the well are unchanged assuming they are correctly determined by a rig-source VSP.

One of the offset-VSP Common Shot Gathers (CSG) from the true models is shown in Fig. 4a, which is bandpass-filtered in the frequency range 6–18 Hz. The red and green dashed lines represent the reflected and transmitted *P*-to-*S* converted waves from the boundary of the high wave speed body. Inverting these data by elastic FWI, we obtain the inverted *P*- and *S*-wave speed models shown in Figs 5a and 5b, respectively. The synthetic data from the inverted models are displayed in Fig. 4b, and waveforms match the observed data well. The model updates are shown in Figs 5c and 5d. There, the black dashed lines show the region recovered by elastic FWI. The wave speed models are more reliably updated at the receiver side because of their dense spacing. We can see that elastic FWI of the offset-VSP data can give accurate wave speed updates for the target anticline structure, both in terms of the strong wave speed contrast and its correct location. The inverted *S*-wave speed model is more accurate than the *P*-wave speed model owing to *P*-to-*S* converted waves from the target anticline, and the overburden wave speed variations in the offset-VSP data. See, for example, the *P*-to-*S* events marked by the red and green lines in Fig. 4a.

We migrate the multi-component offset-VSP data by elastic RTM using the FWI-derived elastic models. The V_P and V_S images are shown in Figs 6a and 6b, respectively. We can see that the V_P image contains a strong low-wavenumber component, and that the V_S image has a higher resolution than the V_P image for the target structure by virtue of the *P*-to-*S* converted waves. In this case, the V_S images seem to be better suited for structural interpretation of the target area than the V_P images.

FIELD DATA

We next apply 2D elastic FWI to the real offset-VSP dataset. The source is generated by a vibrator with sweep frequencies ranging from 6 Hz to 64 Hz. The initial V_P and V_S models in Figs 7a and 7b are obtained by rig-source VSP data analysis, traveltime modeling of the offset VSP *P*-to-*P* events and conventional reflection tomography of the surface seismic data. The dashed black lines show boundaries of large wave speed contrasts in initial models.

We first use travel-time inversion to build initial V_P and V_S models. The STF is assumed to be a Klauder wavelet. Then, we bandpass the data by a low-pass filter (8 Hz), and apply elastic FWI to the early-arrival waveforms. Next, the STF is updated according to eq. (5). After early-arrival FWI, we reduce data muting to proceed to the elastic FWI of the late-arrivals. The inverted V_P and V_S models are shown in Figs 7c and 7d, respectively. We migrate the VSP data using the initial and inverted elastic models. The stacked V_S images are shown in Figs 8a and 8b, respectively. We can see that the V_S image from the inverted model is more in focus than that from the initial model (red arrows). This indicates that elastic FWI has improved the models.

CONCLUSION

We have demonstrated the application of isotropic elastic FWI to an onshore offset-VSP data set over a structurally complex geological target. A practical elastic FWI workflow is developed. The results of the numerical tests indicate that elastic FWI of offset-VSP data can give accurate wave speed updates for the target anticline structure. The elastic RTM images show that the V_S image has a higher resolution than the V_P image for the target structure thanks to the *P*-to-*S* converted events which can be exploited for the elastic imaging.

ACKNOWLEDGMENTS

The authors thank DNO for providing financial support and for permission to publish this work. Computational resources were made available through the Princeton Institute for Computational Science and Engineering (PICSciE).

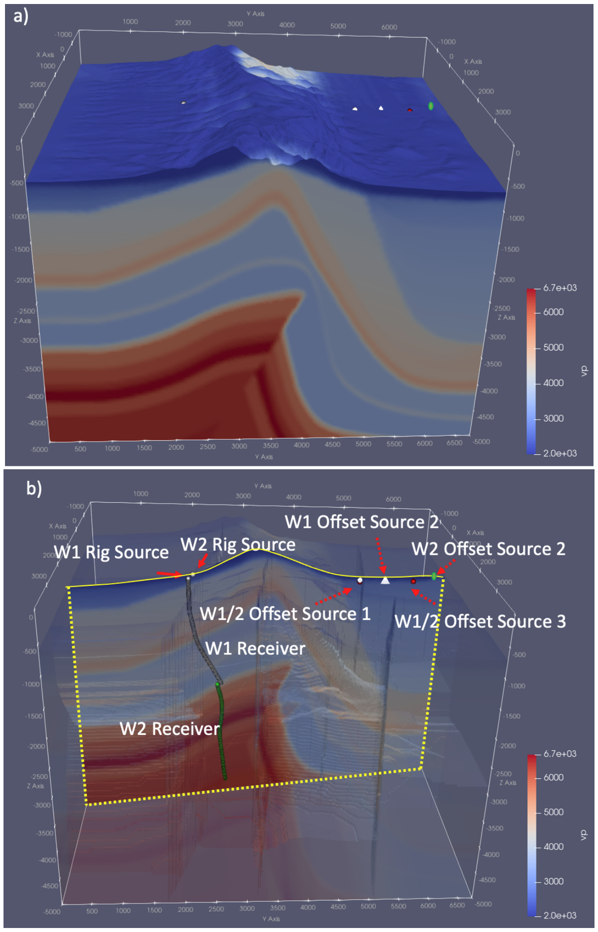

Figure 1: An anticlinal structure with a complex overburden and strong topography. (a) A 3D P-wave speed model. (b) A 2D wave speed slice near wells W1 and W2. Sources and receivers are marked as shown.

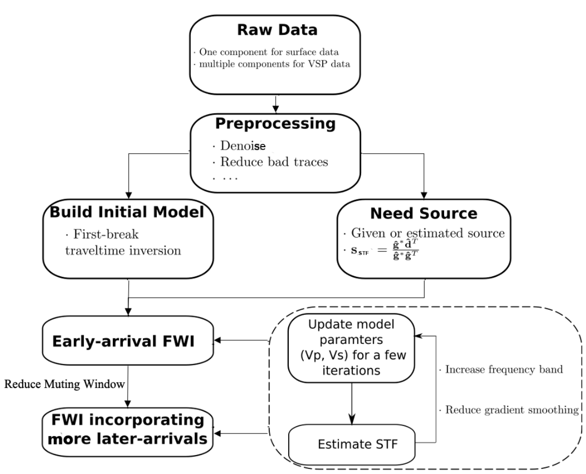

Figure 2: Workflow of elastic FWI followed in this paper.

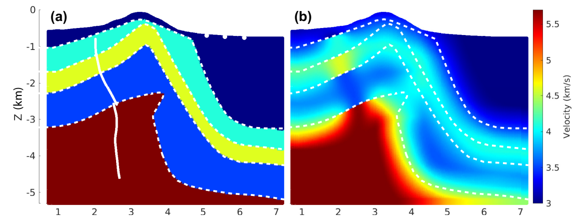

Figure 3: (a) True and (b) initial V_P models used in the synthetic elastic FWI test. White dots and lines in (a) represent offset sources and VSP receiver locations, respectively. Dashed white lines highlight boundaries of different layers.

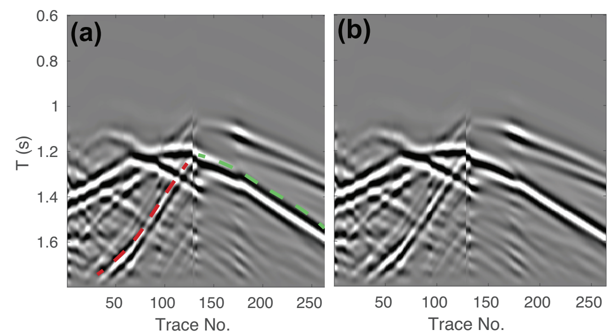

Figure 4: Vertical-component data calculated from the (a) true and (b) inverted wave speed models. In (a), we mark the reflected (red) and transmitted (green) P-to-S converted waves generated by the boundaries of the high wave speed body.

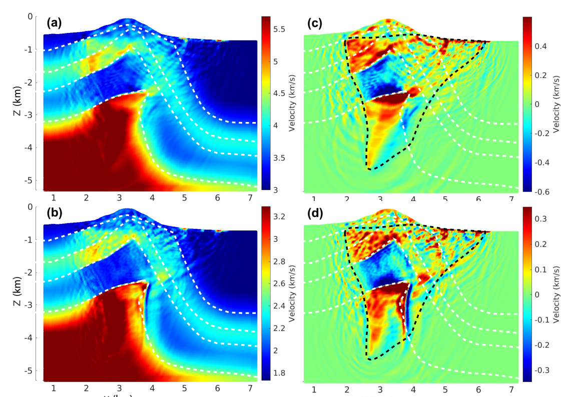

Figure 5: (a) V_P and (b) V_S models inverted by elastic FWI in the synthetic test. Dashed white lines represent the boundaries of different layers in the true model. (c) V_P and (d) V_S model updates by elastic FWI, with the dashed black lines showing the recovered region.

10.1190/segam2021-3582871.1

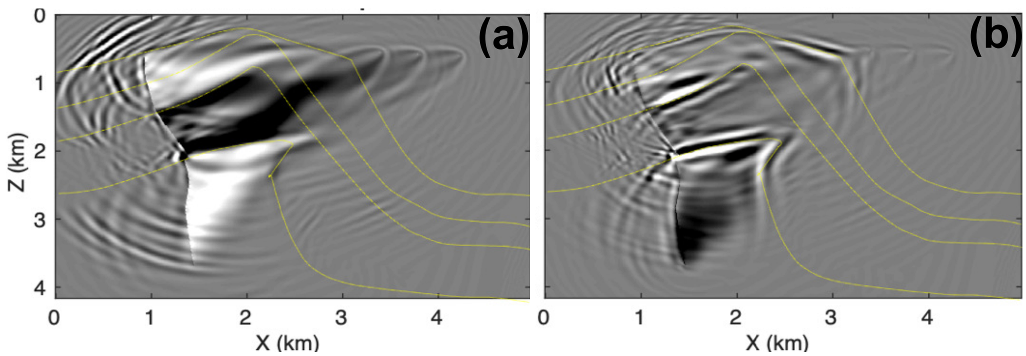

Figure 6: (a) V_P and (b) V_S images generated by elastic RTM of the synthetic data using the inverted models.

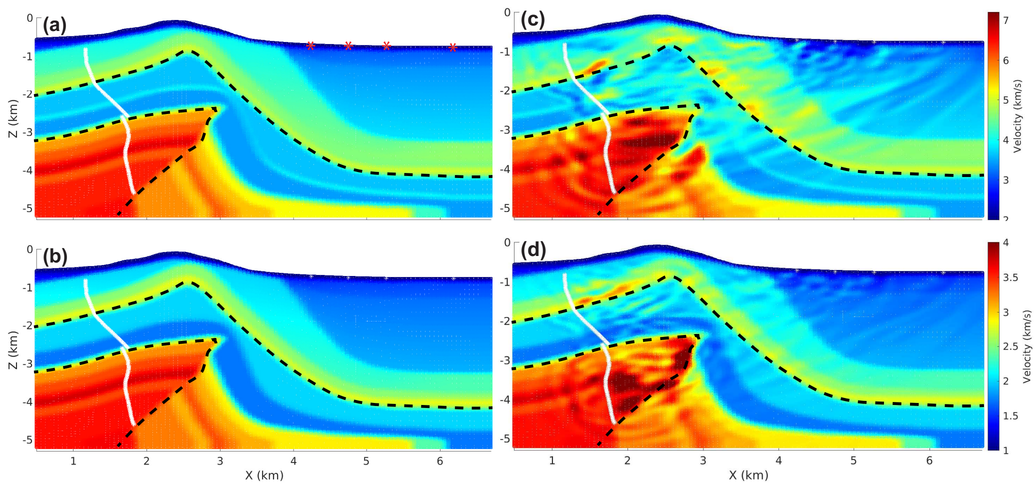

Figure 7: Initial (a) V_P and (b) V_S models for inversion of real data. Inverted (c) V_P and (d) V_S models obtained by elastic FWI. The dashed black lines show boundaries of large wave speed contrasts in the initial model. The downhole receiver locations are marked in white, while the offset-VSP source locations are marked by red asterisks.

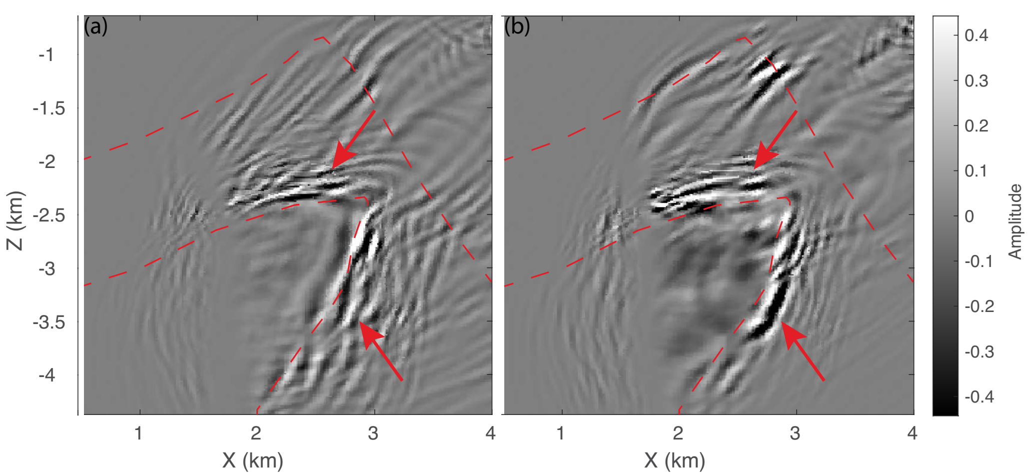

Figure 8: Stacked V_S images obtained by elastic RTM using the (a) initial and (b) inverted models. The dashed red lines show boundaries of large wave speed contrasts in the initial model. The arrows highlight the differences between (a) and (b).

REFERENCES

Borisov, D., F. Gao, P. Williamson, and J. Tromp, 2020, Application of 2D full-waveform inversion on exploration land data: Geophysics, **85**, no. 2, R75–R86, doi: https://doi.org/10.1190/geo2019-0082.1.

Bunks, C., F. M. Saleck, S. Zaleski, and G. Chavent, 1995, Multiscale seismic waveform inversion: Geophysics, **60**, 1457–1473, doi: https://doi.org/10.1190/1.1443880.

Choi, Y., and T. Alkhalifah, 2012, Application of multi-source waveform inversion to marine streamer data using the global correlation norm: Geophysical Prospecting, **60**, 748–758, doi: https://doi.org/10.1111/j.1365-2478.2012.01079.x.

Hinds, R. C., N. L. Anderson, and R. D. Kuzmiski, 1996, VSP interpretive processing: Theory and practice: SEG, doi: https://doi.org/10.1190/1.9781560801894.

Komatitsch, D., and J. Tromp, 1999, Introduction to the spectral element method for three-dimensional seismic wave propagation: Geophysical Journal International, **139**, 806–822, doi: https://doi.org/10.1046/j.1365-246x.1999.00967.x.

Lailly, P., 1983, The seismic inverse problem as a sequence of before stack migrations: Conference on Inverse Scattering: Theory and Application, SIAM, 206–220.

Modrak, R. T., D. Borisov, M. Lefebvre, and J. Tromp, 2018, SeisFlows — Flexible waveform inversion software: Computers & Geosciences, **115**, 88–95, doi: https://doi.org/10.1016/j.cageo.2018.02.004.

Murphy, G., V. Brown, and D. Vigh, 2020, Land FWI in the Delaware Basin, west Texas: A case study: The Leading Edge, **39**, 324–331, doi: https://doi.org/10.1190/tle39050324.1.

Nocedal, J., and S. J. Wright, 2006, Numerical optimization: Springer. Operations Research and Financial Engineering.

Pérez Solano, C., and R. É. Plessix, 2019, Velocity-model building with enhanced shallow resolution using elastic waveform inversion — An example from onshore Oman: Geophysics, **84**, no. 6, R977–R988, doi: https://doi.org/10.1190/geo2018-0736.1.

Sen, M. K., and P. L. Stoffa, 1990, Nonlinear seismic waveform inversion in one dimension using simulated annealing: Geophysics, **56**, 1119–1122, doi: https://doi.org/10.1190/1.1889926.

Tarantola, A., 1984, Inversion of seismic reflection data in the acoustic approximation: Geophysics, **49**, 1259–1266, doi: https://doi.org/10.1190/1.1441754.

Tromp, J., C. Tape, and Q. Liu, 2005, Seismic tomography, adjoint methods, time reversal and banana-doughnut kernels: Geophysical Journal International, **160**, 195–216, doi: https://doi.org/10.1111/j.1365-246X.2004.02453.x.